RSC Advances

PAPER

Immobilized copper-layered nickel ferrite on acid-activated montmorillonite, [(NiFe$_2$O$_4$@Cu)(H$^+$-Mont)], as a superior magnetic nanocatalyst for the green synthesis of xanthene derivatives

Behzad Zeynizadeh [ID] * and Soleiman Rahmani

In this study, the immobilization of copper-layered nickel ferrite on the surface and in the cavities of acid-activated montmorillonite (H$^+$-Mont) was investigated. In this context, magnetic nanoparticles (MNPs) of NiFe$_2$O$_4$ as the prime magnetic cores were prepared. Next, through the reduction of Cu^{2+} ions with sodium borohydride, the nanoparticles of Cu^0 were immobilized on the nanocore-surface of NiFe$_2$O$_4$, and the constituent NiFe$_2$O$_4$@Cu MNPs were obtained. Moreover, through the activation of montmorillonite K10 (Mont K10) with HCl (4 M) under controlled conditions, the H$^+$-Mont constituent was prepared. The nanostructured NiFe$_2$O$_4$@Cu was then intercalated within the interlayers and on the external surface of the H$^+$-Mont constituent to afford the novel magnetic nanocomposite (NiFe$_2$O$_4$@Cu)(H$^+$-Mont). The prepared clay nanocomposite was characterized using FTIR spectroscopy, SEM, EDX, XRD, VSM and BET analyses. The obtained results showed that through acid-activation, the stacked-sheet structure of Mont K10 was exfoliated to tiny segments, leading to a significant increase in the surface area and total pore volume of the H$^+$-Mont constituent as compared to those of montmorillonite alone. SEM analysis also exhibited that the dispersion of NiFe$_2$O$_4$@Cu MNPs in the interlayers and on the external surface of acid-activated montmorillonite was carried out successfully, and the nanoparticle sizes were distributed in the range of 15–25 nm. The BET surface analysis also indicated that through the immobilization of NiFe$_2$O$_4$@Cu MNPs, the surface area and total pore volume of the H$^+$-Mont system were decreased. The catalytic activity of (NiFe$_2$O$_4$@Cu)(H$^+$-Mont) was further studied towards the synthesis of substituted 13-aryl-5*H*-dibenzo[*b,i*]xanthene-5,7,12,14(13*H*) tetraones **3(a–k)** and 3,3,6,6-tetramethyl-9-aryl-3,4,5,6,7,9-hexahydro-1*H*-xanthene-1,8(2*H*) diones **5(a–k)** *via* the pseudo-one-pot three-component cyclocondensation of 2-hydroxy-1,4-naphthoquinone (Lawsone)/dimedone and aromatic aldehydes in a mixture of H$_2$O–EtOH (1 : 1 mL) as a green solvent at 80–90 °C. The (NiFe$_2$O$_4$@Cu)(H$^+$-Mont) MNPs can be easily separated from the reaction mixture by an external magnetic field and reused for seven consecutive cycles without significant loss of catalytic activity.

1. Introduction

Among O-containing heterocyclic compounds, xanthene derivatives are very important. These materials have attracted significant attention of many pharmacologists and synthetic chemists due to their broad spectrum of biological properties such as insecticidal, antifungal and urease activity,[1] analgesic,[2] antiinflammatory,[2] anti-bacterial,[3] antioxidant,[4] and antiproliferative activity,[5] trypanothione reductase (TryR) inhibition,[6] chloroquine (CQ) potentiation,[6] and antimalarial[6] and anticancer activity.[7] Moreover, some xanthene materials have been used as antagonists for paralyzing the action of zoxalamine[8] and dyes,[9–11] in laser technology,[12] as pH-sensitive fluorescent agents[13] and as bactericides in agriculture.[14] These

capabilities indicate the significant impact of xanthenes as the source of valuable drugs and rationalize the immense interest of numerous researchers towards their synthesis; a literature review has shown that using Fe$_3$O$_4$,[15] ZrO$_2$,[16] silica sulfuric acid,[17] (HPO$_3$)$_n$,[18] HOAc,[19] HClO$_4$/SiO$_2$,[20] PPA/SiO$_2$,[20] SbCl$_3$/SiO$_2$,[21] silica chloride,[22] NaHSO$_4$·SiO$_2$,[22] FeCl$_3$/SiO$_2$,[23] InCl$_3$,[18] InCl$_3$·4H$_2$O/ionic liquid,[24] In(OTf)$_3$,[25] SO$_4$$^{2-}$/TiO$_2$,[26] Fe$_3O_4$@SiO$_2$@SO$_3$H,[27] Fe$_3O_4$@TiO$_2$@SO$_3$-H,[28] ZrO$_2$@SO$_3$H,[29] *n*-Bu$_4HSO_4$,[30] [Hmim]TFA,[31] *p*-dodecylbenzenesulfonic acid,[32] *p*-dodecylbenzenesulfonic acid/ultrasound,[33] Dowex-50W,[34] amberlyst-15,[35] montmorillonite K10,[36] Fe^{3+}-montmorillonite,[37] 1,1,3,3-*N,N,N',N'*-tetramethylguanidinium trifluoroacetate/TFA,[38] Et$_3$(PhCH$_2$)NBr,[39] TMSCl,[40] DABCO,[41] CuI/poly(4-vinylpyridine),[42] graphene oxide-incorporated strontium NPs,[43] choline chloride/itaconic acid,[44] (NH$_4$)$_2$HPO$_4$,[45] and polyaniline-*p*-toluenesulfonate[46] 1,8-dioxo-octahydroxanthenes have been prepared. In this context, some procedures involving Dowex-50W,[34]

Faculty of Chemistry, Urmia University, Urmia 5756151818, Iran. E-mail: bzeynizadeh@gmail.com

1,1,3,3-N,N,N',N'-tetramethylguanidinium trifluoroacetate/TFA,[38] graphene oxide-incorporated strontium NPs,[43] choline chloride/itaconic acid,[44] [Msim]Cl,[47] [Hmim][HSO$_4$],[47] [Et$_3$N–SO$_3$H]Cl,[47] [Et$_3$NH][HSO$_4$],[47] H$_2$SO$_4$,[48] [Bmim][HSO$_4$],[48] [Bmim][BF$_4$],[49] N-sulfonic acid poly(4-vinylpyridinium) hydrogen sulfate,[50] p-toluene sulfonic acid,[51] amberlyst-15,[52] and FeCl$_3$·6H$_2$O[53] have also been reported for the preparation of 5H-dibenzo[b,i]xanthene tetraone materials. Aligned with the manifold capabilities of xanthene derivatives, therefore, the development of simple, efficient and clean synthetic protocols using green and highly reactive environmental benign catalysts is still needed.

Previously reported studies indicate the usefulness of Cu nanoparticles because of their low cost, high thermal and electrical conductivity, antifungal and antibacterial properties, and catalytic activity in organic synthesis; Cu is the most commonly investigated transition metal elements.[54–59] In spite of the great convenience of Cu NPs, however, they have a strong tendency to agglomerate as well as a high affinity to react with air oxygen. These characteristics extensively diminish the surface areas and catalytic activities of copper nanoparticles. In order to overcome the mentioned drawbacks, the immobilization of Cu NPs on the surface of solid supports, especially magnetically nanoparticles (MNPs) of metal oxides, may be a prime choice. Among the various magnetic metal oxides, NiFe$_2$O$_4$ MNPs have attracted the attention of scientists due to their excellent magnetic, physical and electrical properties and high thermal stability (up to 900 °C) as well as their usefulness in drug delivery, ferrofluids, pigments, microwave devices, gas sensors and catalysts.[60–64] In this area, the immobilization of copper nanoparticles on nickel ferrite (NiFe$_2$O$_4$@Cu) was successfully reported for the efficient reduction of nitroarenes to arylamines with NaBH$_4$.[65] Observation of the results reveals that because of the synergic influences of copper element and the core magnetic material, this type of immobilization dramatically accelerates the rates of reduction reactions. Moreover, feasible and efficient separation of the applied catalyst system from the reaction mixture can be carried out using an external magnetic field.

Clay minerals of the smectite group, such as montmorillonite K10 (Mont K10), are considered to be ecofriendly and suitable solid supports on which metal nanoparticles can be stabilized in the interlamellar spaces.[66–68] Mont K10 is a stacked-sheet clay mineral that belongs to the family of 2 : 1 phyllosilicates. It is composed of one sandwiched-Al^{3+} octahedral sheet between two Si^{4+} tetrahedral sheets[69] and has several advantages in terms of high surface area, swelling, cation exchange ability, low cost, ease of handling and non-corrosiveness.[70] This micro/mesoporous material, in both its natural and modified forms, possesses both Brønsted and Lewis acid characteristics. Although montmorillonite K10 possesses inherent acidity, further activation of montmorillonite with strong acids such as HCl can exfoliate the adjacent sheets to tiny segments, leading to dramatic increases in surface area and Brønsted acidity as well as the generation of numerous pores with micro/meso dimensions.[71]

A literature review shows that the synthesis of xanthene materials catalyzed by copper nanoparticles has not yet been investigated. Therefore, in line with the outlined strategies

and in continuation of our research program towards the synthesis and application of magnetic nanocatalysts,[65,72–76] herein, we wish to introduce the immobilization of copper-layered nickel ferrite on acid-activated montmorillonite, (NiFe$_2$O$_4$@Cu)(H$^+$-Mont) (Fig. 1), with the aims of (i) combining the catalytic activity of the copper-layered nickel ferrite constituent with the Brønsted and Lewis acidity of the H$^+$-Mont clay mineral, affording prominent catalytic activity of the final catalyst system and (ii) avoiding aggregation and improving the stability of the copper nanoparticles as well as the shelf life capability of the NiFe$_2$O$_4$@Cu MNPs via immobilization in the interlamellar spaces of the clay mineral. Further examination indicated that the prepared nanostructured (NiFe$_2$O$_4$@Cu)(H$^+$-Mont) exhibited excellent catalytic activity towards the one-pot Knoevenagel reaction of 2-hydroxy-1,4-naphthoquinone (Lawsone)/dimedone with aromatic aldehydes in a mixture of H$_2$O–EtOH (1 : 1 mL) as a green solvent to afford 5H-dibenzo[b,i]xanthene tetraones and hexahydroxanthene diones (Fig. 2).

2. Experimental

2.1. Instruments and reagents

All chemicals were purchased from chemical companies, were of the best quality and were used without further purification. ^{1}H, ^{13}C NMR and FT-IR spectra were recorded on 300 MHz Bruker Avance and Thermo Nicolet Nexus 670 spectrometers. Melting points were recorded on an Electrothermal 9100 melting point apparatus and are uncorrected. TLC was applied to monitor the reactions over silica gel-coated 60 F254 aluminum sheets. The magnetic properties of the nanocatalysts were measured using vibration sample magnetometer (VSM, Meghnatis Daghigh Kavir Co., Iran) analysis under an external magnetic field of up to 20 kOe. The morphologies and size distributions of the nanoparticles were examined by scanning electron microscopy (SEM) using an FESEM-TESCAN MIRA3 instrument. X-ray diffraction (XRD) measurements were carried out on X'PertPro Panalytical diffractometer (Holland) at 40 kV and 30 mA with Cu Kα radiation ($\lambda = 1.5418$ Å). Signal data were recorded from $2\theta = 10°$ to $80°$ with a step interval of $0.05°$.

2.2. Synthesis of NiFe$_2$O$_4$ MNPs

A mixture of Ni(OAc)$_2$·4H$_2$O, Fe(NO$_3$)$_3$·9H$_2$O, NaOH and NaCl in a molar ratio of 1 : 2 : 8 : 2, respectively, was ground for 60 min in
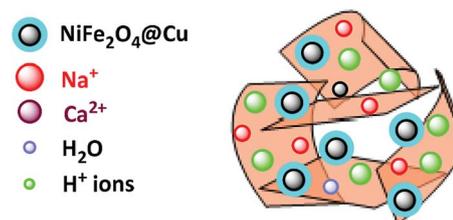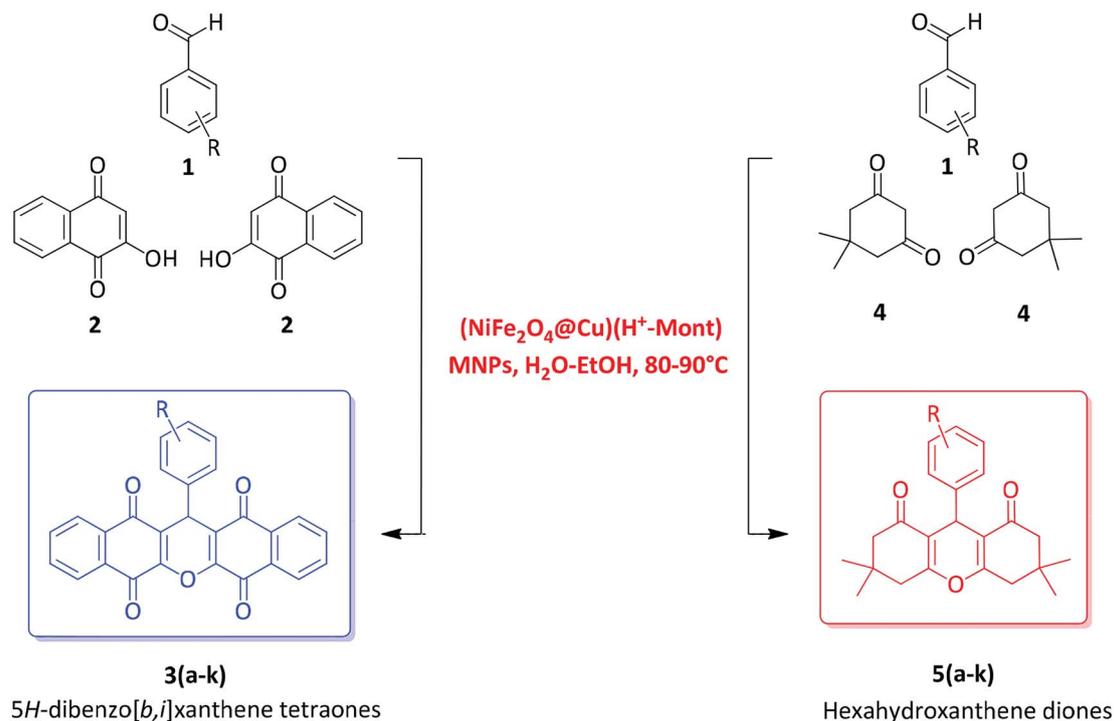

Fig. 1 Magnetic nanoparticles of (NiFe$_2$O$_4$@Cu)(H$^+$-Mont).

Fig. 2 Synthesis of xanthene materials catalyzed by (NiFe$_2$O$_4$@Cu)(H$^+$-Mont) MNPs.

the absence of solvent. The reaction was exothermic and was accompanied by the release of heat. When the reaction was complete, the mixture was washed several times with deionized water to remove NaCl and residual contaminants, followed by drying at 80 °C for 10 h. The resulting powder was calcinated at 900 °C for 2 h to obtain magnetic nanoparticles of NiFe$_2$O$_4$.[65]
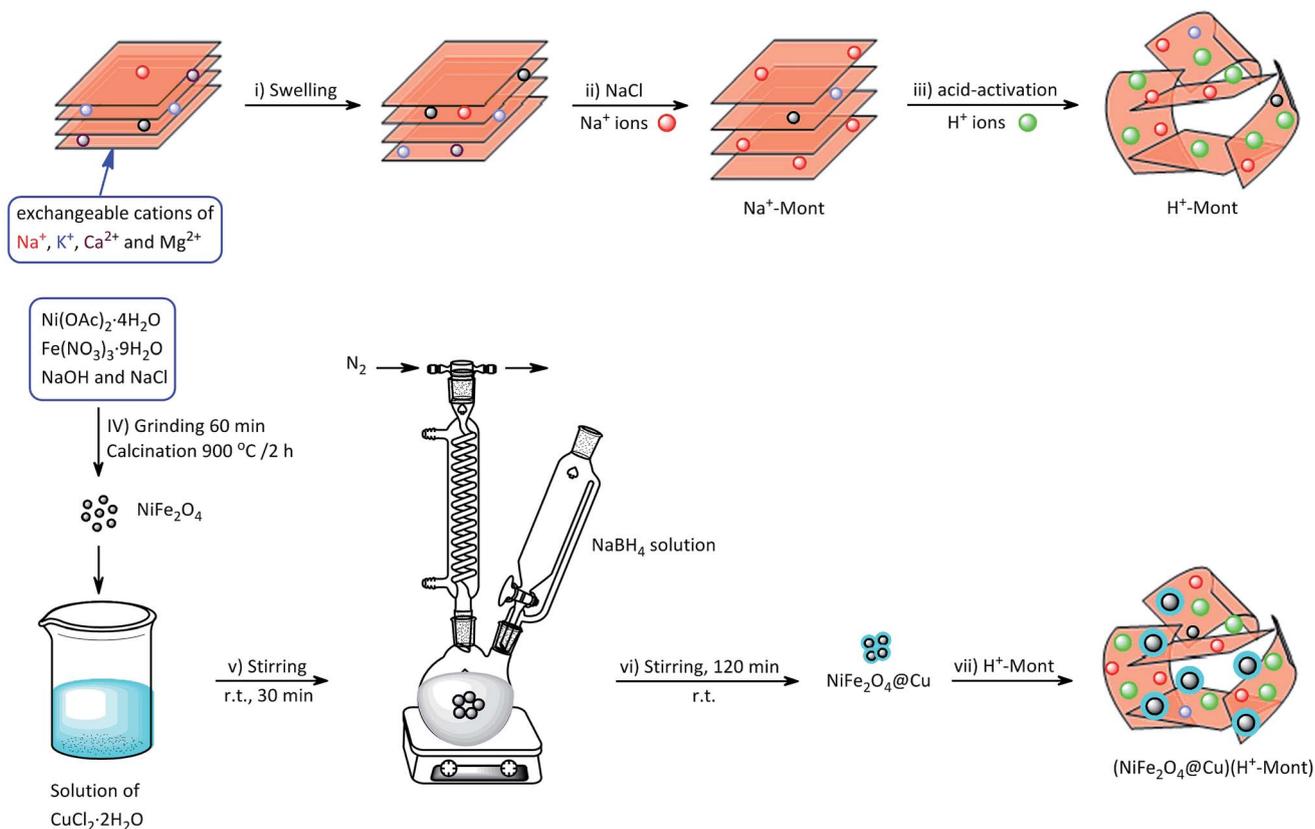

Fig. 3 Preparation of the (NiFe$_2$O$_4$@Cu)(H$^+$-Mont) MNPs.
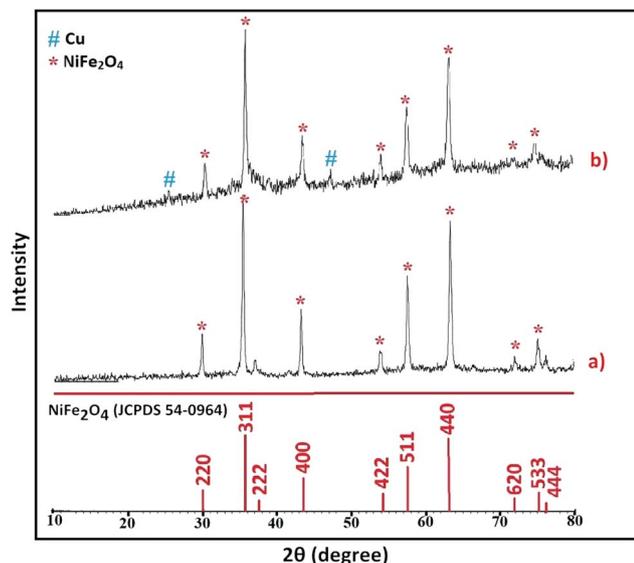
Fig. 4 XRD patterns of (a) $NiFe_2O_4$ and (b) the $NiFe_2O_4@Cu$ MNPs.

2.3. Synthesis of $NiFe_2O_4@Cu$ MNPs

A mixture of $NiFe_2O_4$ (1 g) containing an aqueous solution of $CuCl_2 \cdot 2H_2O$ (0.25 g in 30 mL H_2O) was prepared. The resulting mixture was stirred for 30 min at room temperature; $NaBH_4$ (0.11 g in 30 mL H_2O) was then added dropwise over 20 min (N_2 atmosphere). The mixture was then stirred for 2 h. After that, the magnetic nanoparticles of $NiFe_2O_4@Cu$ were separated by magnetic decantation and then washed with ethanol and deionized water. Drying under air atmosphere afforded $NiFe_2O_4@Cu$ MNPs.[65]

2.4. Preparation of homoionic Na^+-exchanged montmorillonite (Na^+-Mont)

To a beaker containing an aqueous solution of NaCl (2 M, 200 mL), montmorillonite K10 (10 g) was added, and the mixture was stirred vigorously for 2 h at room temperature. The mixture was then allowed to settle, and the aqueous phase was decanted. Then, the solid residue was again charged with an aqueous solution of NaCl (2 M, 200 mL). The procedure was repeated 3 more times. Finally, the aqueous phase was decanted and the solid residue was washed frequently with distilled water until the conductivity of the liquid filtrate reached the conductivity of distilled water. The resulting product was then dried at 50 °C in an oven to afford homoionic Na^+-exchanged montmorillonite (Na^+-Mont).[74]

2.5. Preparation of acid-activated montmorillonite (H^+-Mont)

To a round-bottom flask containing an aqueous solution of HCl (4 M, 100 mL), Na^+-Mont (5 g) was added. The resulting dispersion was stirred under reflux conditions for 2 h. After cooling, the mixture was filtered, and the resulting montmorillonite was washed frequently with distilled water to remove any Cl^- ions from the clay mineral (tested with $AgNO_3$). The

acid-activated clay was collected and dried in an oven (50 °C) to afford acid-activated montmorillonite (H^+-Mont).[76]

2.6. Synthesis of $(NiFe_2O_4@Cu)(H^+$-Mont) MNPs

Individual suspensions of H^+-Mont (4.2 g) in deionized water (200 mL; the pH value of the resulting suspension was adjusted to ~5 by 3 wt% HCl) and $NiFe_2O_4@Cu$ (2.1 g) in deionized water (200 mL; the pH value of the resulting suspension was adjusted to ~9 by 3 wt% aqueous ammonia) were irradiated by ultrasound for 30 min. The two suspensions were combined, followed by stirring for 2 h. The clay nanocomposite, $(NiFe_2O_4@Cu)(H^+$-Mont), was separated by magnetic decantation and then washed with EtOH. Drying under air atmosphere afforded the final product in a weight ratio of 2 : 1 for $NiFe_2O_4@Cu : H^+$-Mont.

2.7. Determining the cation-exchange capacity (CEC) of the clay minerals

The cation-exchange capacities (CEC) of the clay minerals were measured through a reported procedure.[77] In this context, a clay mineral (such as Mont K10) (0.5 g) was dispersed in a standard alcoholic solution of $CaCl_2$ (10 mL, 0.05 M) and the prepared mixture was stirred at room temperature for 24 h. The suspension was filtered, washed with EtOH (20 mL) and dried at room temperature for 12 h. The Ca^{2+}-exchanged clay mineral
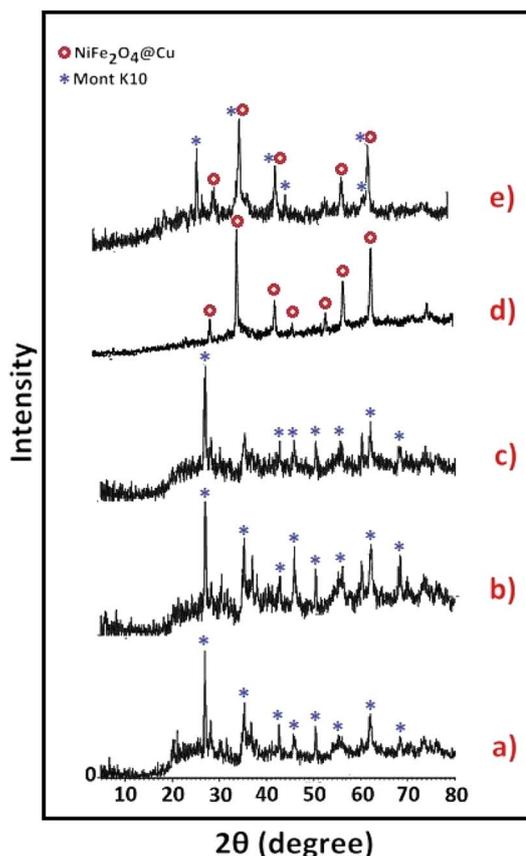

Fig. 5 XRD patterns of (a) Mont K10, (b) Na^+-Mont, (c) H^+-Mont, (d) $NiFe_2O_4@Cu$ and (e) $(NiFe_2O_4@Cu)(H^+$-Mont).
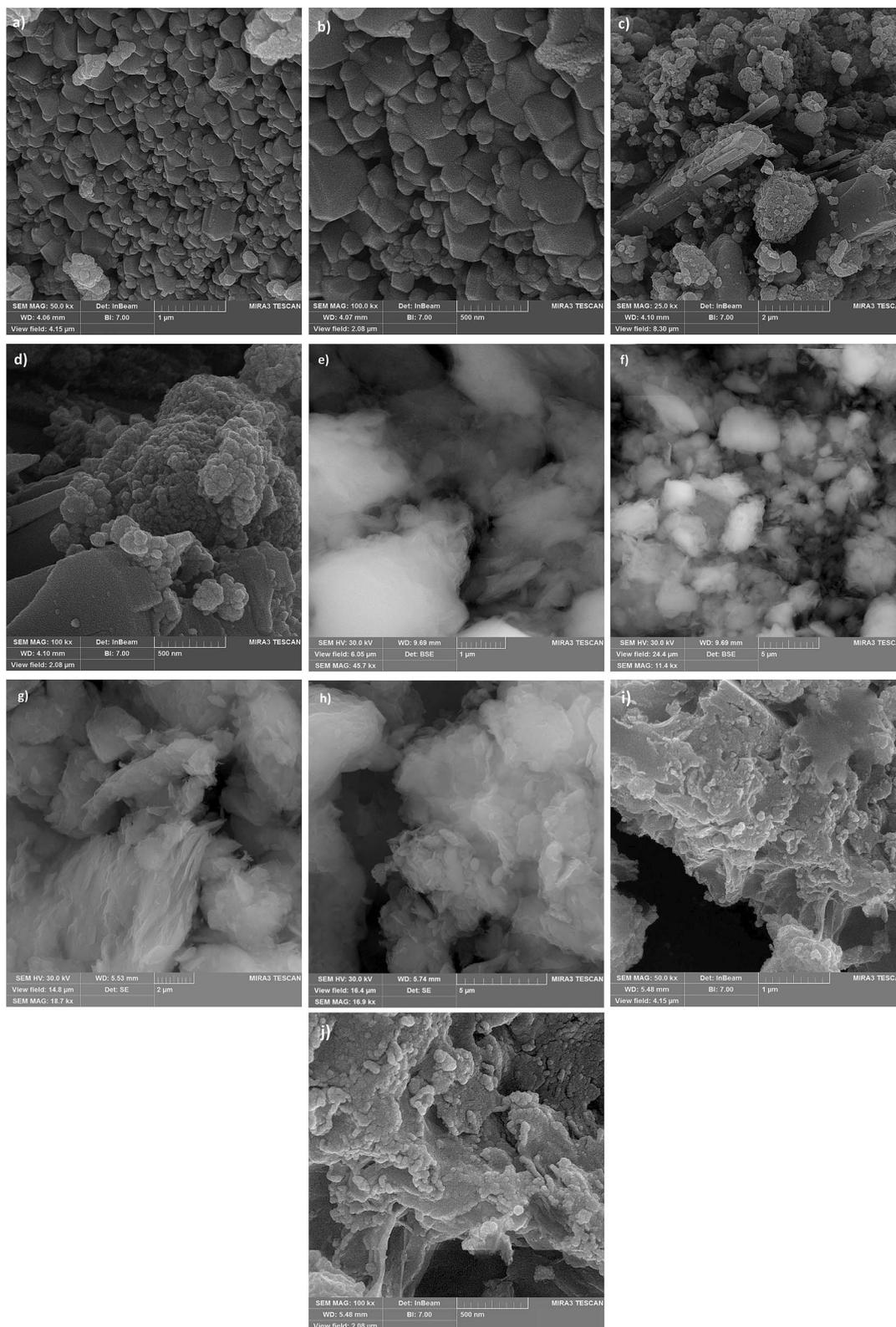
Fig. 6 SEM images of $NiFe_2O_4$ (a and b), $NiFe_2O_4$@Cu (c and d), Mont K10 (e and f), H^+-Mont (g and h) and $(NiFe_2O_4$@Cu$)(H^+$-Mont) (i and j).

was then transferred to a volumetric flask (250 mL). By adding distilled water, the volume of the flask was increased to the standard limit (250 mL). The amount of Ca^{2+} was determined by titration with a standard solution of EDTA. The difference in the concentrations of Ca^{2+} before and after cation-exchange processing afforded the CEC (meq. g^{-1}) of the clay mineral.
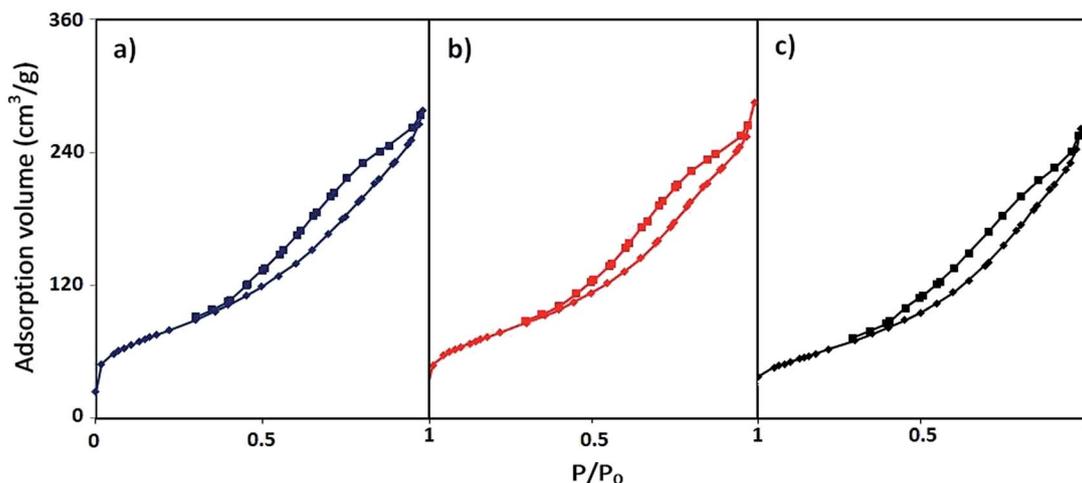
Fig. 7 N$_2$ adsorption–desorption isotherms of the (a) Mont K10, (b) H$^+$-Mont and (c) (NiFe$_2$O$_4$@Cu)(H$^+$-Mont) systems.

2.8. General procedure for the synthesis of 13-aryl-5H-dibenzo[b,i]xanthene-5,7,12,14(13H)-tetraones

In a round-bottom flask (10 mL) equipped with a magnetic stirrer, a mixture of 2-hydroxy-1,4-naphthoquinone (2, 2 mmol), aromatic aldehyde (1, 1 mmol) and (NiFe$_2$O$_4$@Cu)(H$^+$-Mont) (20 mg) in H$_2$O–EtOH (1 : 1 mL) was prepared. The resulting mixture was stirred at 80 °C for a particular time, as mentioned in Table 4. The progress of the reaction was monitored by TLC (eluent, n-hexane/EtOAc: 10/4). After completion of the reaction, EtOAc (3 mL) was added, and stirring of the reaction mixture was continued for 5 min. The nanocatalyst was then separated from the reaction mixture by an external magnetic field. After that, the organic layer was separated from the aqueous solution. Evaporation of the solvent under reduced pressure afforded the crude 5H-dibenzo[b,i]xanthene tetraone. Further purification could be carried out by recrystallization from hot EtOH, affording the products 3(a–k) in 70% to 98% yields. Selected spectral data for the products are given as follows:

2.8.1. 13-Phenyl-5H-dibenzo[b,i]xanthene-5,7,12,14(13H)-tetraone (3a). FT-IR (KBr, ν cm^{-1}): 3346, 1651, 1594, 1360, 1267, 1043, 725; ^{1}H NMR (300 MHz, CDCl$_3$): δ (ppm) 6.26 (s, 1H, CH), 7.21–7.34 (s, 4H, Ar), 7.65–7.79 (m, 4H, Ar), 8.08–8.19 (m, 5H, Ar); ^{13}C NMR (75 MHz, CDCl$_3$): δ (ppm) 32.2, 122.6, 129.6, 132.7, 137.9, 154.8, 181.3, 184.7.

2.8.2. 13-(2-Chlorophenyl)-5H-dibenzo[b,i]xanthene-5,7,12,14(13H)-tetraone (3b). FT-IR (KBr, ν cm^{-1}): 3267, 1638, 1591, 1464, 1354, 1267, 1035, 971, 725, 643; ^{1}H NMR (300 MHz, CDCl$_3$): δ (ppm) 6.09 (s, 1H, CH), 7.12–7.25 (m, 2H, Ar), 7.28–7.38 (m, 2H, Ar), 7.74–7.86 (m, 4H, Ar), 7.86–8.06 (m, 4H, Ar).

2.8.3. 5H-Dibenzo[b,i]xanthene-5,7,12,14(13H)-tetraone (3d). FT-IR (KBr, ν cm^{-1}): 3071, 1676, 1602, 1351, 1263, 1209, 968, 942, 770, 735; ^{1}H NMR (300 MHz, CDCl$_3$): δ (ppm) 2.49 (s, 2H, CH$_2$), 7.71–7.85 (m, 4H, Ar), 7.95–7.97 (m, 4H, Ar).

2.8.4. 13-(4-Methoxyphenyl)-5H-dibenzo[b,i]xanthene-5,7,12,14(13H)-tetraone (3e). FT-IR (KBr, ν cm^{-1}): 3345, 3071, 2932, 1654, 1594, 1468, 1361, 1275, 1041, 730, 464; ^{1}H NMR (300 MHz, CDCl$_3$): δ (ppm) 3.77 (s, 3H, OCH$_3$), 6.35 (s, 1H, CH), 6.84–6.94 (m, 2H, Ar), 7.11–7.18 (m, 1H, Ar), 7.21–7.29 (m, 1H, Ar), 7.64–7.80 (m, 4H, Ar), 8.04–8.15 (m, 4H, Ar); ^{13}C NMR (75 MHz, CDCl$_3$): δ (ppm) 33.12, 54.1, 122.8, 125.5, 126.2, 126.6, 128.1, 128.6, 129.5, 132.9, 135.1, 154.1, 157.4, 181.5, 184.1.

2.8.5. 13-(p-Tolyl)-5H-dibenzo[b,i]xanthene-5,7,12,14(13H)-tetraone (3g). FT-IR (KBr, ν cm^{-1}): 3174, 3013, 1638, 1585, 1382, 1347, 1275, 1218, 973, 880, 736, 666; ^{1}H NMR (300 MHz, CDCl$_3$): δ (ppm) 3.79 (s, 3H, CH$_3$), 6.18 (s, 1H, CH), 6.83 (d, 2H, Ar), 7.21 (d, 2H, Ar), 7.65–7.79 (m, 4H, Ar), 8.07–8.15 (m, 4H, Ar); ^{13}C NMR (75 MHz, CDCl$_3$): δ (ppm) 36.9, 113.8, 122.9, 126.3, 127.2, 128.1, 129.6, 129.8, 132.7, 132.2, 135.0, 154.7, 158.4, 181.3, 184.7.

2.8.6. 13-(2-Hydroxyphenyl)-5H-dibenzo[b,i]xanthene-5,7,12,14(13H)-tetraone (3h). FT-IR (KBr, ν cm^{-1}): 3222, 1641, 1589, 1480, 1354, 1237, 1041, 975, 728; ^{1}H NMR (300 MHz, DMSO-d6): δ (ppm) 5.74 (s, 1H, CH), 7.08–7.29 (m, 4H, Ar), 7.70–7.98 (m, 8H, Ar), 11.48 (bs, 1H, OH).

Table 1 Surface properties of the examined clay composite systems

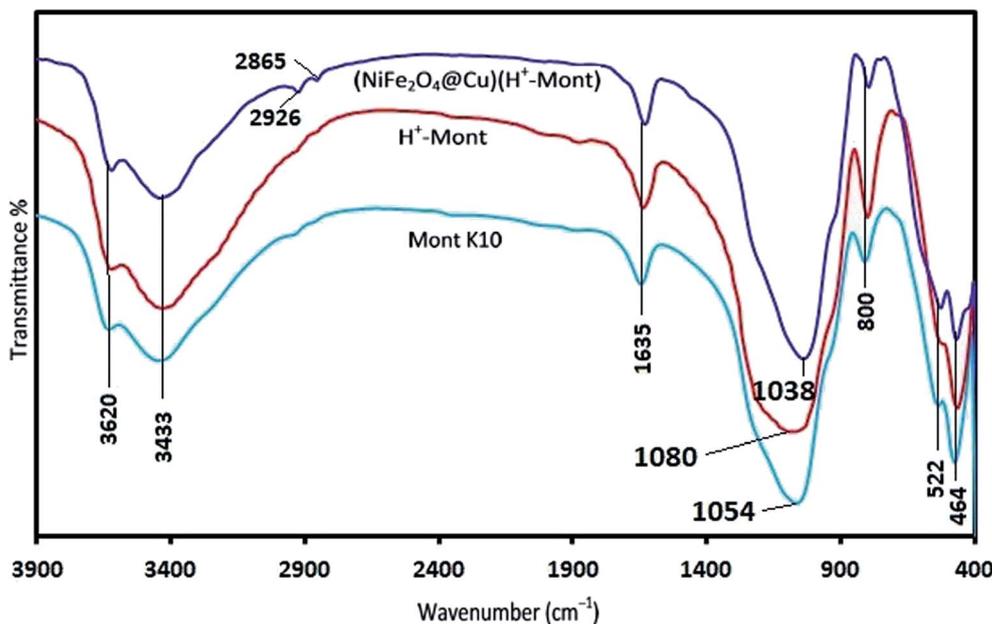| Sample	S_{BET} (m^2 g^{-1})	V_m (cm^3 g^{-1})	Average pore diameter (nm)	V_p (cm^3 g^{-1})	Total pore volume (cm^3 g^{-1})
Mont K10	250.11	51.835	6.427	0.4016	0.4298
H$^+$-Mont	280.52	50.313	6.7483	0.419	0.5081
(NiFe$_2$O$_4$@Cu)(H$^+$-Mont)	119.52	27.461	7.9242	0.2326	0.2368
NiFe$_2$O$_4$@Cu	14.84	3.41	34.74	0.128	0.129

Fig. 8 FT-IR spectra of the Mont K10, H$^+$-Mont and (NiFe$_2$O$_4$@Cu)(H$^+$-Mont) systems.

2.8.7. 13-(4-Nitrophenyl)-5H-dibenzo[b,i]xanthene-5,7,12,14(13H)-tetraone (3i). FT-IR (KBr, ν cm^{-1}): 3330, 2923, 2859, 1654, 1592, 1519, 1346, 1265, 1038, 724; ^{1}H NMR (300 MHz, CDCl$_3$): δ (ppm) 6.38 (s, 1H, CH), 7.31–7.36 (m, 1H, Ar), 7.44–7.51 (m, 1H, Ar), 7.71–7.84 (m, 5H, Ar), 8.08–8.18 (m, 5H, Ar).

2.8.8. 13-(3-Nitrophenyl)-5H-dibenzo[b,i]xanthene-5,7,12,14(13H)-tetraone (3j). FT-IR (KBr, ν cm^{-1}): 3337, 2923, 1654, 1594, 1526, 1349, 1267, 1035, 726; ^{1}H NMR (300 MHz, CDCl$_3$): δ (ppm) 6.25 (s, 1H, CH), 7.42–7.48 (m, 1H, Ar), 7.63–7.84 (m, 6H, Ar), 8.10–8.19 (m, 5H, Ar).

2.8.9. 13-(4-Pyridyl)-5H-dibenzo[b,i]xanthene-5,7,12,14(13H)-tetraone (3k). FT-IR (KBr, ν cm^{-1}): 3463, 2918,

2852, 1671, 1597, 1499, 1351, 1268, 1159, 944, 803, 724, 574; ^{1}H NMR (300 MHz, CDCl$_3$): δ (ppm) 2.94 (s, 1H, CH), 6.78 (bs, 2H, Pyridyl), 7.64–8.01 (m, 8H, Ar), 8.62 (d, 2H, Pyridyl).

2.9. General procedure for the synthesis of 3,3,6,6-tetramethyl-9-aryl-3,4,5,6,7,9-hexahydro-1H-xanthene-1,8(2H)-diones

Synthesis of hexahydroxanthene diones was carried out using the procedure described in Section 2.8 with dimedone (4, 2 mmol) at 90 °C. Selected spectral data for the products are given as follows:

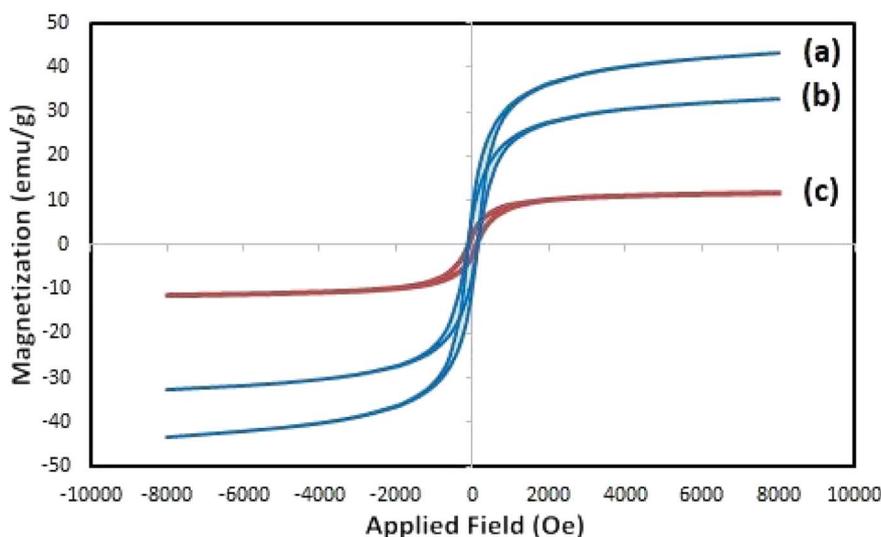**2.9.1. 3,3,6,6-Tetramethyl-9-phenyl-3,4,5,6,7,9-hexahydro-1H-xanthene-1,8(2H)-dione (5a).** FT-IR (KBr, ν cm^{-1}): 2949,

Fig. 9 Magnetization curves of (a) NiFe$_2$O$_4$, (b) NiFe$_2$O$_4$@Cu and (c) the (NiFe$_2$O$_4$@Cu)(H$^+$-Mont) MNPs.

Table 2 Optimization experiments for the synthesis of 13-(4-chlorophenyl)-5H-dibenzo[b,i]xanthene-5,7,12,14(13H)-tetraone (**3c**) catalyzed by (NiFe$_2$O$_4$@Cu)(H$^+$-Mont) MNPs^a

Entry	Nanocatalyst (mg)	Solvent (2 mL)	Temp. (°C)	Time (min)	Yield^b (%)
1	—	EtOH	60	240	5
2	—	H$_2$O	60	240	5
3	20	EtOH	60	45	60
4	20	H$_2$O	60	30	70
5	20	EtOH–H$_2$O (1 : 1)	60	30	85
6	20	DMF	60	120	40
7	20	EtOAc	60	120	50
8	20	CH$_3$CN	60	120	55
9	20	Solvent-free	60	120	60
10	20	EtOH–H$_2$O (1 : 1)	r.t.	120	60
11	20	EtOH–H$_2$O (1 : 1)	80	20	95
12	10	EtOH–H$_2$O (1 : 1)	80	20	70
13	30	EtOH–H$_2$O (1 : 1)	80	120	75

^{a} The condensation reactions were carried out with 2-hydroxy-1,4-naphthoquinone (2 mmol) and 4-chlorobenzaldehyde (1 mmol). ^{b} Isolated yield.

1662, 1650, 1363, 1350, 1197, 1163, 1143, 997, 700; ^{1}H NMR (300 MHz, CDCl$_3$): δ (ppm) 0.99 (s, 6H, 2Me), 1.10 (s, 6H, 2Me), 2.13–2.23 (d, 4H, 2CH$_2$), 2.43 (s, 4H, 2CH$_2$), 4.69 (s, 1H, CH), 6.98–7.31 (m, 5H, Ar).

2.9.2. 9-(2-Chlorophenyl)-3,3,6,6-tetramethyl-3,4,5,6,7,9-hexahydro-1H-xanthene-1,8(2H)-dione (5b). FT-IR (KBr, ν cm^{-1}): 2952, 2636, 1723, 1628, 1381, 1241, 838, 757; ^{1}H NMR (300 MHz, CDCl$_3$): δ (ppm) 1.02 (s, 6H, 2Me), 1.10 (s, 6H, 2Me), 2.18 (s, 4H, 2CH$_2$), 2.45 (s, 4H, 2CH$_2$), 5.01 (s, 1H, CH), 7.00–7.26 (m, 4H, Ar).

2.9.3. 9-(4-Chlorophenyl)-3,3,6,6-tetramethyl-3,4,5,6,7,9-hexahydro-1H-xanthene-1,8(2H)-dione (5c). FT-IR (KBr, ν cm^{-1}): 2953, 2881, 1665, 1472, 1388, 1195, 1153, 1010, 834, 759; ^{1}H NMR (300 MHz, CDCl$_3$): δ (ppm) 1.00 (s, 6H, 2Me), 1.11 (s, 6H, 2Me), 2.14–2.28 (s, 4H, 2CH$_2$), 2.47 (s, 4H, 2CH$_2$), 4.72 (s, 1H, CH), 7.17–7.27 (m, 4H, Ar).

2.9.4. 9-(2-Methoxyphenyl)-3,3,6,6-tetramethyl-3,4,5,6,7,9-hexahydro-1H-xanthene-1,8(2H)-dione (5h). FT-IR (KBr, ν cm^{-1}): 2951, 1724, 1661, 1487, 1368, 1242, 1195, 1143, 831, 759; ^{1}H NMR (300 MHz, CDCl$_3$): δ (ppm) 0.91 (s, 6H, 2Me), 1.04 (s, 6H, 2Me), 2.12 (s, 4H, 2CH$_2$), 2.37 (s, 4H, 2CH$_2$), 3.72 (s, 3H, OCH$_3$), 4.82 (s, 1H, CH), 6.82–7.35 (m, 3H, Ar).

2.9.5. 9-(2-Hydroxyphenyl)-3,3,6,6-tetramethyl-3,4,5,6,7,9-hexahydro-1H-xanthene-1,8(2H)-dione (5i). FT-IR (KBr, ν cm^{-1}): 2951, 2829, 1721, 1627, 1379, 1239, 1161, 1026, 877, 754; ^{1}H NMR (300 MHz, CDCl$_3$): δ (ppm) 1.01 (s, 6H, 2Me), 1.04 (s, 6H, 2Me), 1.96 (s, 2H, CH$_2$), 2.34–2.38 (s, 4H, 2CH$_2$), 2.34–2.64 (s, 4H, 2CH$_2$), 4.68 (s, 1H, CH), 7.01–7.27 (m, 4H, Ar), 10.47 (bs, 1H, OH).

2.9.6. 3,3,6,6-Tetramethyl-9-(4-nitrophenyl)-3,4,5,6,7,9-hexahydro-1H-xanthene-1,8(2H)-dione (5j). FT-IR (KBr, ν cm^{-1}): 2950, 2875, 2631, 1599, 1514, 1363, 1259, 1155, 851; ^{1}H NMR (300 MHz, CDCl$_3$): δ (ppm) 0.81 (s, 6H, 2Me), 0.95 (s, 6H, 2Me), 2.01–2.16 (s, 4H, 2CH$_2$), 2.47 (s, 4H, 2CH$_2$), 4.54 (s, 1H, CH), 7.73 (s, 2H, Ar), 8.01 (s, 2H, Ar).

2.9.7. 3,3,6,6-Tetramethyl-9-(3-nitrophenyl)-3,4,5,6,7,9-hexahydro-1H-xanthene-1,8(2H)-dione (5k). FT-IR (KBr, ν cm^{-1}): 2954, 2882, 1668, 1600, 1527, 1456, 1359, 1192, 1145, 752; ^{1}H NMR (300 MHz, CDCl$_3$): δ (ppm) 0.99 (s, 6H, 2Me), 1.11 (s, 6H, 2Me), 2.13–2.28 (s, 4H, 2CH$_2$), 2.51 (s, 4H, 2CH$_2$), 4.83 (s, 1H, CH), 7.37–8.03 (m, 4H, Ar).

3. Results and discussion

3.1. Synthesis and characterization of (NiFe$_2$O$_4$@Cu)(H$^+$-Mont) MNPs

Synthesis of the (NiFe$_2$O$_4$@Cu)(H$^+$-Mont) MNPs was carried out through a seven-step procedure: (i) swelling (hydration) of montmorillonite K10 by vigorous stirring of the clay mineral in distilled water. Due to this process, Mont K10 can absorb water between its interlamellar spaces; hence, the stacked sheets of the clay mineral move apart. The swelling expands the surface area of montmorillonite and exposes the cations of the interlayers to contribute Brønsted and Lewis acidity character;[70] (ii) stirring of the swelled montmorillonite in an aqueous solution of NaCl to afford homoionic Na$^+$-exchanged montmorillonite. Through simple ion-exchange, many cations of the interlayers in montmorillonite K10 are exchanged with Na$^+$ ions. The diffusion of Na$^+$ ions endows the clay mineral with a high capacity for exchanging Na$^+$ ions with various guest species (transition metals, complexes and H$^+$ ions). In other words, the ions are encapsulated in the interlamellar spaces; therefore, the acidity (Brønsted and Lewis) of the clay mineral can be changed for different purposes; (iii) stirring of the homoionic Na$^+$-exchanged Mont in an aqueous solution of HCl to afford acid-activated Mont; (iv) preparation of NiFe$_2$O$_4$ MNPs via solid state grinding of Ni(OAc)$_2$·4H$_2$O and Fe(NO$_3$)$_3$·9H$_2$O in the presence of NaOH; (v) mixing of NiFe$_2$O$_4$ MNPs with an aqueous solution of CuCl$_2$·2H$_2$O; (vi) reduction of Cu^{2+} ions to Cu^0 with NaBH$_4$ to afford NiFe$_2$O$_4$@Cu MNPs; and finally, (vii)

Table 3 Comparison of the catalytic activity of (NiFe$_2$O$_4$@Cu)(H$^+$-Mont) MNPs with those of other potentially active species in the synthesis of dibenzo[b,i]xanthene tetraone **3c**^{a}

Entry	Catalyst^a	Time (min)	Yield^b (%)
1	Cu^0 NPs	60	70
2	NiFe$_2$O$_4$	60	65
3	NiFe$_2$O$_4$@Cu	60	70
4	Mont K10	60	60
5	H$^+$-Mont	60	80
6	Na$^+$-Mont	60	60
7	(NiFe$_2$O$_4$@Cu)(H$^+$-Mont)	20	95

^{a} All reactions were carried out in H$_2$O–EtOH (1 : 1 mL) under oil bath (80 °C) conditions using 20 mg of the nanocatalyst. ^{b} Isolated yield.

preparation of $(NiFe_2O_4@Cu)(H^+\text{-Mont})$ MNPs *via* simple mixing of the individual sonicated suspensions of $NiFe_2O_4@Cu$ and $H^+\text{-Mont}$ constituents (Fig. 3). In this context, through the electrostatic attraction of $NiFe_2O_4@Cu$ (positive charge) to H^+-Mont (negative charge) compartments and the repulsion within the H^+-Mont layers/segments, nanosegments of $NiFe_2O_4@Cu$ are dispersed on the surface and in the interlamellar spaces of the H^+-Mont constituent.

The concentration of exchangeable cations in a clay mineral is called the cation exchange capacity (CEC), and it is measured in milli-equivalents per 100 g of dried clay.[77] The measured CEC results for the Mont K10 and Na^+-Mont clays were 85 and 110 meq. g^{-1}, respectively, representing the successful replacement of Na^+ ions instead of other cations in the interlamellar spaces of the clay minerals.

3.2. Characterization of the $(NiFe_2O_4@Cu)(H^+\text{-Mont})$ MNPs

3.2.1. XRD analysis. The phase purities and structural elucidation of the $NiFe_2O_4$, $NiFe_2O_4@Cu$, Mont K10, Na^+-Mont, H^+-Mont and $(NiFe_2O_4@Cu)(H^+\text{-Mont})$ systems were studied using wide-angle X-ray diffraction analysis (Fig. 4 and 5). In the diffractogram of $NiFe_2O_4$ (Fig. 4a), the peaks at $2\theta = 30.40°$, $35.77°$, $37.40°$, $43.51°$, $54.21°$, $57.60°$, $63.11°$, $71.90°$, $75.20°$ and $76.05°$ correspond to the (2 2 0), (3 1 1), (2 2 2), (4 0 0), (4 2 2), (5 1 1), (4 4 0), (6 2 0), (5 3 3) and (4 4 4) reflection planes of standard cubic spinel $NiFe_2O_4$ (JCPDS 54-964), respectively, showing the high phase purity and crystallinity of the prepared sample. In this context, the XRD pattern of $NiFe_2O_4@Cu$ MNPs (Fig. 4b) shows that in addition to the reflection planes of $NiFe_2O_4$, the

peaks present at $2\theta = 27.40°$ and $48.02°$ can be attributed to the reflection planes of copper species. The XRD pattern of montmorillonite K10 (Fig. 5a) also shows that along with *hkl* and two-dimensional *hk* reflections, the commercial clay mineral contains impurities of quartz, cristobalite and feldspar. Moreover, analysis of the pattern of homoionic Na^+-exchanged montmorillonite (Fig. 5b) reveals that the intensity of the reflection peaks notably increased. This increase is attributed to the diffusion of Na^+ ions in the interlamellar spaces of the clay mineral *via* ion-exchange processing.[78,79] Despite this, the XRD pattern of the H^+-Mont (Fig. 5c) system shows a decrease in the intensity of the reflection peaks. This can be attributed to exfoliation/destruction of layers in the Na^+-Mont clay during HCl-activation.[80] In continuation, the XRD pattern of $(NiFe_2O_4@Cu)(H^+\text{-Mont})$ (Fig. 5e) shows that upon combining the $NiFe_2O_4@Cu$ and H^+-Mont constituents, no structural changes occurred in the clay matrix, and the pattern of the nanocomposite contains the characteristic peaks of both compartments.

3.2.2. SEM analysis. The morphologies and size distributions of the particles in the prepared $NiFe_2O_4$, $NiFe_2O_4@Cu$, Mont K10, H^+-Mont and $(NiFe_2O_4@Cu)(H^+\text{-Mont})$ systems were investigated by scanning electron microscopy (SEM). The SEM images of $NiFe_2O_4$ (Fig. 6a and b) and $NiFe_2O_4@Cu$ (Fig. 6c and d) present that the morphologies of the two MNPs are quite different: $NiFe_2O_4$ is composed of polygon/irregular segments, resulting in surfaces with low porosity and a size distribution of the particles in the range of 10 to 25 nm. The SEM images of $NiFe_2O_4@Cu$ show that through the immobilization of copper nanoparticles on the surface of $NiFe_2O_4$, the porosity of the

Table 4 Preparation of dibenzo[*b,i*]xanthene tetraones catalyzed by $(NiFe_2O_4@Cu)(H^+\text{-Mont})$ MNPs[a]

Entry	R-	Product	Time (min)	Yield[b] (%)	Mp (°C)[43,44,48,50] Found	Reported
1	C_6H_5	**3a**	40	90	305–306	305–307 (ref. 43 and 44)
2	2-ClC_6H_4	**3b**	30	92	308–309	307–309 (ref. 43 and 48)
3	4-ClC_6H_4	**3c**	20	95	331–332	330–332 (ref. 43 and 48)
4	H	**3d**	30	97	306–308	—
5	4-MeOC_6H_4	**3e**	40	78	319–321	320–322 (ref. 43 and 48)
6	3-MeOC_6H_4	**3f**	35	75	>330	—
7	4-MeC_6H_3	**3g**	70	80	305–307	304–307 (ref. 44)
8	2-OHC_6H_4	**3h**	60	70	217–219	218–220 (ref. 44)
9	$4\text{-O}_2NC_6H_4$	**3i**	70	98	312–313	312–313 (ref. 50)
10	$3\text{-O}_2NC_6H_4$	**3j**	75	95	340–341	340–342 (ref. 43 and 44)
11	4-Pyridyl	**3k**	80	92	>320	—

[a] All reactions were carried out with a molar ratio of aryl aldehyde : 2-hydroxy-1,4-naphthoquinone of 1 : 2 in the presence of 20 mg of the nanocatalyst in H_2O–EtOH (1 : 1 mL, 80 °C). [b] Yield refers to isolated pure product.

surface was extensively increased, and the nanocomposite is constituted of agglomerated tiny spherical segments. Moreover, the particle sizes are distributed in the range of 10 to 40 nm.

SEM images of Mont K10 and acid-activated Mont are also illustrated in Fig. 6e–h. Comparison of the images shows that through the acid-activation, the stacked sheets of Mont K10 were exfoliated into tiny segments. This phenomenon can be interpreted by the major elimination of Al^{3+} and $Fe^{2+/3+}$ contents from the octahedral sites when the activation of montmorillonite with HCl was carried out. Moreover, through the elimination of Al^{3+} and $Fe^{2+/3+}$ ions from the interlayers, numerous pores on the surface and internal sheets of montmorillonite were generated, increasing the surface area of the H^+-Mont system. In this context, the depicted SEM images of the $(NiFe_2O_4@Cu)(H^+$-Mont) MNPs (Fig. 6i and j) present that the nanocatalyst is composed of stacked-sheet structures containing agglomerated rough/irregular segments. The sizes of the particles in the $(NiFe_2O_4@Cu)(H^+$-Mont) system are distributed in the range of 18 to 25 nm. The SEM analysis also exhibited that anchoring of the $(NiFe_2O_4@Cu)$ constituent on the surface of the clay compartment was carried out successfully, leading to a decrease of the surface porosity in comparison to that of the $NiFe_2O_4@Cu$ MNPs.

3.2.3. N₂ adsorption–desorption analysis. Nitrogen adsorption–desorption analysis is commonly utilized to study the specific surface areas of nanocomposite systems. In addition, information regarding the pore sizes and total pore volumes of nanomaterials is accessible using this analysis. In this area, Fig. 7 shows the N_2 adsorption–desorption profiles for the Mont K10, H^+-Mont and $(NiFe_2O_4@Cu)(H^+$-Mont) systems. Based on BDDT IUPAC classification, the shapes of the isotherms for all samples are closer to that of isotherm IV, with H3 hysteresis loops in the desorption profiles. This type of isotherm is characteristic of micro/mesoporous materials.[81]

In this context, the surface properties of the Mont K10, H^+-Mont, $(NiFe_2O_4@Cu)(H^+$-Mont) and $NiFe_2O_4@Cu$ systems, including S_{BET} ($m^2 g^{-1}$), V_m ($cm^3 g^{-1}$), average pore diameter (nm), V_p ($cm^3 g^{-1}$) and total pore volume ($cm^3 g^{-1}$), are summarized in Table 1. Investigation of the results indicates that the surface area and total pore volume of H^+-Mont notably increased *versus* those of Mont K10 alone. This phenomenon is attributed to the exfoliation of stacked sheets to tiny segments and the formation of numerous new pores, affording increases of the pore volume and specific surface area.[82,83] In contrast, anchoring $NiFe_2O_4@Cu$ MNPs on the H^+-Mont compartments decreases the surface area and total pore volume, while the average pore radius of the particles was found to increase. This is attributed to physical occupancy of some of the pores in montmorillonite K10 by $NiFe_2O_4@Cu$ MNPs.[84]

3.2.4. FT-IR analysis. FT-IR is a sensitive tool that was utilized to elucidate the structures as well as the functional groups of the Mont K10, H^+-Mont and $(NiFe_2O_4@Cu)(H^+$-Mont) materials (Fig. 8). The absorption band at 3620 cm^{-1} for Mont K10 is attributed to the vibration of hydroxyl groups bonded to Si^{4+}, Al^{3+} or Mg^{2+} ions. The absorption bands at 3433 and 1635 cm^{-1} show the H–O–H stretching and bending vibrations of the adsorbed water in the interlayers of montmorillonite, and the bands at 522 and 464 cm^{-1} correspond to the bending vibrations of Si–O–Al and Si–O–Si, respectively.[85–87] In this context, comparison of the FT-IR patterns of the Mont K10 and H^+-Mont systems reveals that through the acid-activation of montmorillonite by HCl, the position of the strong band at 1054 cm^{-1} (showing the stretching vibration of Si–O in

Table 5 Preparation of tetramethylxanthene diones using $(NiFe_2O_4@Cu)(H^+$-Mont) MNPs[a]

Ar-CHO **1** + 2 **4** → $(NiFe_2O_4@Cu)(H^+$-Mont) / H_2O:EtOH (1:1), 90 °C → **5(a-k)**

Entry	Ar-	Product	Time (min)	Yield[b] (%)	Mp (°C)[16,19,43] Found	Reported
1	C_6H_5	**5a**	50	90	202–204	202–204 (ref. 16)
2	2-ClC_6H_4	**5b**	35	95	226–227	226–228 (ref. 43)
3	4-ClC_6H_4	**5c**	20	96	231–233	230–232 (ref. 16 and 43)
4	$2,4$-$Cl_2C_6H_3$	**5d**	15	97	242–244	243–245 (ref. 19)
5	3-OH, 4-$MeOC_6H_3$	**5e**	50	80	175–177	—
6	4-OH, 3-$MeOC_6H_3$	**5f**	50	75	170–172	—
7	3-$MeOC_6H_4$	**5g**	100	75	176–177	175–178 (ref. 19)
8	2-$MeOC_6H_4$	**5h**	210	60	229–230	230–231 (ref. 16)
9	2-OHC_6H_4	**5i**	80	75	247–249	—
10	4-$O_2NC_6H_4$	**5j**	20	97	222–224	221–223 (ref. 43)
11	3-$O_2NC_6H_4$	**5k**	20	98	174–176	175–177 (ref. 19)

[a] All reactions were carried out under solvent-free conditions. [b] Yields refer to isolated pure products.
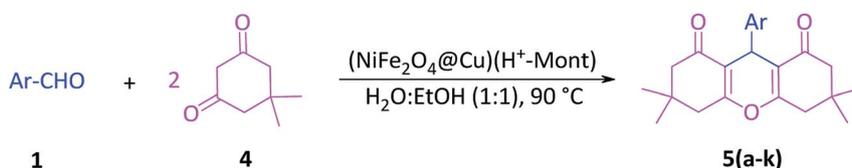
tetrahedral sites) shifted to 1080 cm^{-1}. This fact demonstrates the successful ion-exchange processing of H$^+$-Mont clay. In the case of (NiFe$_2$O$_4$@Cu)(H$^+$-Mont), the stretching vibration of Si–O shifted to 1038 cm^{-1}. This movement is attributed to dispersion of the NiFe$_2$O$_4$@Cu MNPs on the surface and in the interlamellar spaces of the clay constituent. In addition, the bands at 2926 and 2865 cm^{-1} confirmed the immobilization of NiFe$_2$O$_4$@Cu MNPs in the clay matrix through the conformational changes in the metal-linked-clay interactions.[88–90]

3.2.5. VSM analysis. Next, the magnetic behavior of NiFe$_2$O$_4$, NiFe$_2$O$_4$@Cu and the (NiFe$_2$O$_4$@Cu)(H$^+$-Mont) MNPs was studied using vibrating sample magnetometer (VSM) analysis. The magnetization curves of the samples (Fig. 9) present nonlinear reversibility with small hysteresis loops. In addition, the s-shapes shown in the magnetization graphs are characteristic of soft ferromagnetic materials.[91] The magnetization (M_s) values of NiFe$_2$O$_4$ (curve a) and NiFe$_2$O$_4$@Cu (curve b) were found to be 43.458 emu g^{-1} and 33.135 emu g^{-1}, respectively. The decrease in the value of M_s for the NiFe$_2$O$_4$@Cu MNPs is attributed to the presence of diamagnetic copper metal. In this context, due to the existence of the nonmagnetic clay mineral constituent, the saturation magnetization value of the (NiFe$_2$O$_4$@Cu)(H$^+$-Mont) MNPs (curve c) notably decreased to 11.57 emu g^{-1}. This level of magnetization (11.57 emu g^{-1}) is still large enough for magnetic separation.

3.3. Synthesis of xanthene derivatives catalyzed by (NiFe$_2$O$_4$@Cu)(H$^+$-Mont) MNPs

After the successful synthesis and characterization of the (NiFe$_2$O$_4$@Cu)(H$^+$-Mont) MNPs, the catalytic activity of the prepared nanocomposite was further investigated towards the tandem Knoevenagel–Michael reaction of aromatic aldehydes with 2-hydroxy-1,4-naphthoquinone (Lawsone).

The study was primarily carried out by optimizing the condensation reaction of 2-hydroxy-1,4-naphthoquinone (2 mmol) and 4-chlorobenzaldehyde (1 mmol) in the presence and absence of (NiFe$_2$O$_4$@Cu)(H$^+$-Mont) MNPs under different conditions, including changes in the reaction solvent, amount of nanocatalyst and temperature. The results of this investigation are illustrated in Table 2. Observation of the results shows that in the absence of the nanocatalyst, the reaction did not show appropriate efficiency (entries 1 and 2). However, by adding a small amount of (NiFe$_2$O$_4$@Cu)(H$^+$-Mont) MNPs, the rate of the condensation reaction was dramatically accelerated. The examinations also present that among the various solvents, a mixture of H$_2$O–EtOH was the best choice. Moreover, utilizing 20 mg of the nanocatalyst per 1 mmol of 4-chlorobenzaldehyde in a mixture of H$_2$O–EtOH (1 : 1 mL) at 80 °C were the requirements to afford 13-(4-chlorophenyl)-5H-dibenzo[b,i]xanthene-5,7,12,14(13H)-tetraone (**3c**) in 95% isolated yield (Table 2, entry 11), while the reaction was carried out with 100%
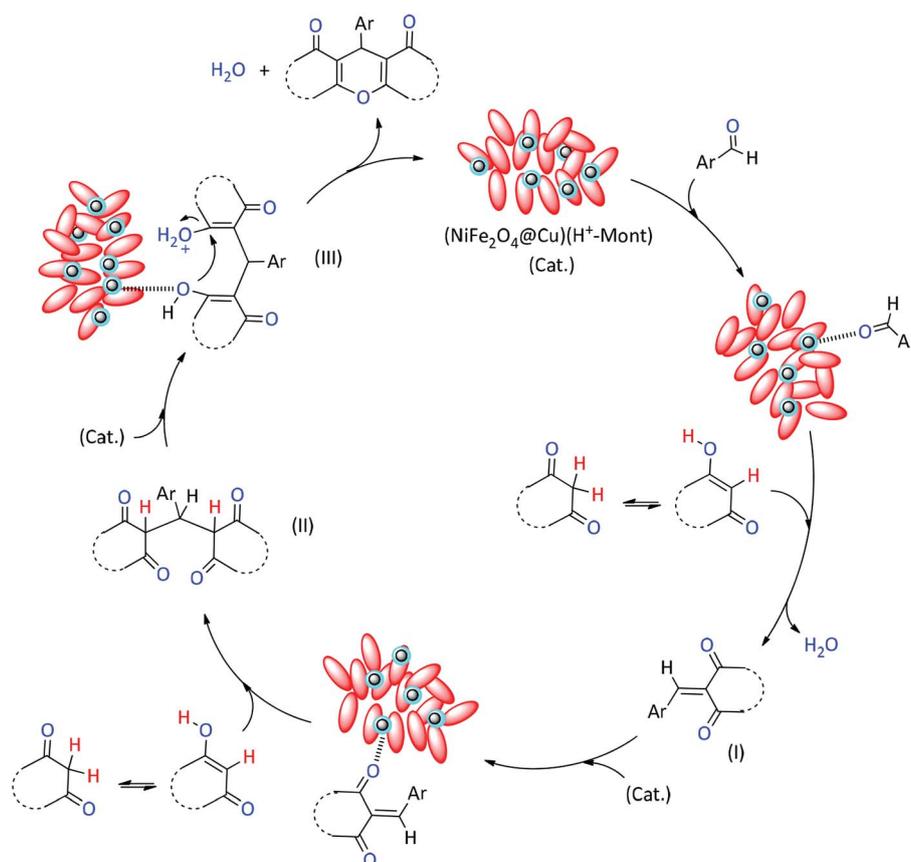

Fig. 10 A proposed mechanism for the Knoevenagel–Michael reaction of aryl aldehydes with 1,3-dicarbonyl compounds catalyzed by (NiFe$_2$O$_4$@Cu)(H$^+$-Mont) MNPs.

Table 6 Synthesis of dibenzo[*b,i*]xanthene tetraone **3c** with (NiFe₂O₄@Cu)(H⁺-Mont) MNPs and other reported promoters

Entry	Catalyst	Time (min)	Yield (%)	Conditions	Temp (°C)	Reusability	Ref.
1	(NiFe₂O₄@Cu)(H⁺-Mont)	20	95	EtOH–H₂O	80	7	*a*
2	Graphene oxide-Sr NPs	105	89	Solvent-free	80	6	43
3	Choline-Cl/itaconic acid	90	90	Ionic liquid	90	5	44
4	[Msim]Cl	5	95	Solvent-free	80	5	47
5	[Hmim][HSO₄]	4	92	Solvent-free	80	5	47
6	[Et₃N–SO₃H]Cl	5	98	Solvent-free	80	5	47
7	[Et₃NH][HSO₄]	4	93	Solvent-free	80	5	47
8	[Bmim][HSO₄]	90	86	EtOH	Reflux	—	48
9	*N*-Sulfonic acid poly(4-vinylpyridinium) HSO₄	15	94	Solvent-free	60	5	50
10	*p*-TSA	150	80	Solvent-free	100	—	51
11	FeCl₃·6H₂O	90	95	Solvent-free	90	—	53

a Present work.

conversion. Investigation of the results also exhibits that although decreasing the loading of the nanocatalyst from 20 mg to 10 mg decreased the yield of condensation reaction (entry 12), increasing the nanocatalyst from 20 mg to 30 mg also diminished the yield from 95% to 75% (entry 13). A possible explanation for the decrease of the yield (utilizing a larger amount of nanocatalyst) is encapsulation/environing of the starting materials by the nanocatalyst, followed by decreasing the inter-collision of the reactants to afford the final product. In summary, the conditions mentioned in entry 11 (Table 2) were selected as the optimum reaction conditions.

In order to clarify the role of nanocatalyst in the synthesis of dibenzo[*b,i*]xanthene tetraone **3c**, the catalytic activity of the (NiFe₂O₄@Cu)(H⁺-Mont) MNPs was compared to those of the potentially active species (Cu⁰ NPs, NiFe₂O₄, NiFe₂O₄@Cu, Mont K10, H⁺-Mont and Na⁺-Mont) under the optimized reaction conditions. The results in Table 3 show that performing the title reaction in the presence of Cu⁰ NPs, NiFe₂O₄@Cu and the modified montmorillonites led to poor yields of **3c**. However, the immobilized NiFe₂O₄@Cu MNPs on acid-activated montmorillonite, (NiFe₂O₄@Cu)(H⁺-Mont), dramatically accelerated the rate of the reaction (Table 3, entry 7).

The capability of (NiFe₂O₄@Cu)(H⁺-Mont) MNPs in the synthesis of dibenzo[*b,i*]xanthene tetraones was further studied towards the one-pot Knoevenagel–Michael reaction of substituted aromatic aldehydes with 2-hydroxy-1,4-naphthoquinone under the optimized reaction conditions. The results of this investigation are illustrated in Table 4. The table reveals that various aryl aldehydes, including electron releasing or withdrawing functionalities, participated successfully in the condensation reaction within 20 to 80 min at 80 °C to afford the corresponding dibenzo[*b,i*]xanthene tetraone materials in high to excellent yields.

The generality of this synthetic method was also studied by examining the condensation reactions of aromatic aldehydes with dimedone as another source of 1,3-dicarbonyl compounds. The obtained results present that the utilized conditions for the synthesis of xanthene materials with 2-hydroxy-1,4-naphthoquinone were also efficient for the case-synthesis with dimedone material. Therefore, substituted aromatic aldehydes (1 mmol) were reacted with dimedone (2 mmol) in the presence of (NiFe₂O₄@Cu)(H⁺-Mont) (20 mg) at 90 °C in a one-pot procedure to afford the cyclization products of 9-aryl-3,3,6,6-tetramethyl-3,4,5,6,7,9-hexahydro-1*H*-xanthene-1,8(2*H*) diones.

Table 7 Synthesis of xanthene dione **5c** catalyzed by (NiFe₂O₄@Cu)(H⁺-Mont) MNPs and other reported promoters

Entry	Catalyst	Time (min)	Yield (%)	Conditions	Temp (°C)	Reusability	Ref.
1	(NiFe₂O₄@Cu)(H⁺-Mont)	20	96	EtOH–H₂O	90	7	*a*
2	ZrO₂ NPs	19	87	Solvent-free	100	—	16
3	HOAc	10	81	Solvent-free	80	—	19
4	NaHSO₄·SiO₂	390	94	CH₃CN	Reflux	—	22
5	Nano Fe₃O₄@TiO₂@SO₃H	40	89	Solvent-free	110	4	28
6	Nano ZrO₂@SO₃H	96	93	Solvent-free	100	5	29
7	[Hmim]TFA	150	93	Ionic liquid	80	4	31
8	Amberlyst-15	300	94	CH₃CN	Reflux	3	35
9	Montmorillonite K10	80	90	Solvent-free	100	—	36
10	Fe³⁺-montmorillonite	360	88	EtOH	Reflux	4	37
11	CuI/poly(4-vinylpyridine)	8	90	Solvent-free	80	8	42
12	Graphene oxide-Sr NPs	60	92	Solvent-free	80	6	43

a Present work.

The results of this investigation are illustrated in Table 5. As can be seen, all reactions were carried out successfully within 15 to 210 min to afford tetramethyl xanthene diones **5(a–k)** in high to excellent yields.

Although the exact mechanism of this synthetic protocol is not clear, a mechanism depicted in Fig. 10 presents the role of $(NiFe_2O_4@Cu)(H^+-Mont)$ MNPs in promoting the formation of xanthene materials. The mechanism shows that the carbonyl moiety of the aryl aldehyde can be activated by the clay nanocatalyst through the existence of numerous Lewis and Brønsted acidity sites. Then, the enolic form of the 1,3-dicarbonyl compound readily reacts with the activated aldehyde to form the Knoevenagel intermediate **I**. Next, through the activation of intermediate **I** with the nanocatalyst followed by Michael addition of the second enole form of 1,3-dicarbonyl material, the intermediate **II** is produced. Through ring closing of the intermediate **II**, finally, the xanthene material is produced.

The usefulness of $(NiFe_2O_4@Cu)(H^+-Mont)$ MNPs in the one-pot syntheses of **3c** and **5c** was also highlighted by a comparison of the obtained results with current and previously reported protocols (Tables 6 and 7). A case study shows that in terms of reaction time, conditions, reusability of the nanocatalyst and yield of the mentioned products, the present work presents a more efficient process than previous systems. On the basis of product yield, solvent-free conditions and rate of the condensation reaction, however, better results with previous systems are observable (Table 6, entries 4–7).

3.4. Recycling of the $(NiFe_2O_4@Cu)(H^+-Mont)$ MNPs

In order to examine the green and economic aspects of $(NiFe_2O_4@Cu)(H^+-Mont)$ MNPs as well as the stability of the $(NiFe_2O_4@Cu)$ moiety on the surface of acid-activated montmorillonite, the reusability of this nanocatalyst towards the synthesis of xanthene material **5c** was also investigated. After completion of the reaction, the nanocatalyst was magnetically separated from the reaction mixture and washed with water and then EtOAc, followed by drying in an oven for use in the next cycle. The obtained results showed that the recycled $(NiFe_2O_4@Cu)(H^+-Mont)$ can be successfully reused at least 7 times without significant loss of its catalytic activity. It is also concluded that after each run, the nature of the clay nanocatalyst remains intact and the $(NiFe_2O_4@Cu)$ moiety is tightly immobilized on the surface of the acid-activated montmorillonite, most probably *via* electrostatic attractions between $NiFe_2O_4$ (positive charge) and the Mont layer (negative charge).

4. Conclusions

In this work, the synthesis of copper-layered nickel ferrite anchored on acid-activated montmorillonite, $(NiFe_2O_4@Cu)(H^+-Mont)$, as a new class of clay composite systems was investigated. The prepared magnetic clay was then characterized using SEM, EDX, XRD, FT-IR, BET and VSM analyses. The catalytic activity of the nanocomposite was also studied towards the synthesis of xanthene derivatives *via* one-pot cyclocondensation of 2-hydroxy-1,4-naphthoquinone (Lawsone)/

dimedone with various aryl aldehydes in a mixture of H_2O–EtOH (1 : 1 mL) as a green solvent at 80 °C to 90 °C, which afforded the products in high to excellent yields. Investigation of the results exhibited that the synergic influence of the copper-layered nickel ferrite constituent with H^+-Mont resulted in a dramatic enhancement of the rate of the reaction. The facile separation of the nanocatalyst by an external magnetic field, generality, short reaction times, high product yields and low loading of the nanocatalyst as well as the excellent reusability of the magnetic clay are the key features which make this synthetic method a prominent choice for the synthesis of xanthenes as biologically active materials.

Conflicts of interest

The authors declare that they do not have any conflict of interest.

Acknowledgements

References

1 J. M. Khurana, D. Magoo, K. Aggarwal, N. Aggarwal, R. Kumar and C. Srivastava, *Eur. J. Med. Chem.*, 2012, **58**, 470–477.

2 H. N. Hafez, M. I. Hegab, I. S. Ahmed-Farag and A. B. A. El-Gazzar, *Bioorg. Med. Chem. Lett.*, 2008, **18**, 4538–4543.

3 O. Evangelinou, A. G. Hatzidimitriou, E. Velali, A. A. Pantazaki, N. Voulgarakis and P. Aslanidis, *Polyhedron*, 2014, **72**, 122–129.

4 A. Ilangovan, K. Anandhan, K. M. Prasad, P. Vijayakumar, R. Renganathan, D. A. Ananth and T. Sivasudha, *Med. Chem. Res.*, 2015, **24**, 344–355.

5 C. Spatafora, V. Barresi, V. M. Bhusainahalli, S. Di Micco, N. Musso, R. Riccio, G. Bifulco, D. Condorelli and C. Tringali, *Org. Biomol. Chem.*, 2014, **12**, 2686–2701.

6 K. Chibale, M. Visser, D. van Schalkwyk, P. J. Smith, A. Saravanamuthu and A. H. Fairlamb, *Tetrahedron*, 2003, **59**, 2289–2296.

7 N. Mulakayala, P. V. N. S. Murthy, D. Rambabu, M. Aeluri, R. Adepu, G. R. Krishna, C. M. Reddy, K. R. S. Prasad, M. Chaitanya, C. S. Kumar, M. V. B. Rao and M. Pal, *Bioorg. Med. Chem. Lett.*, 2012, **22**, 2186–2191.

8 G. Saint-Ruf, H. T. Hieu and J. P. Poupelin, *Naturwissenschaften*, 1975, **62**, 584–590.

9 B. B. Bhowmik and P. Ganguly, *Spectrochim. Acta, Part A*, 2005, **61**, 1997–2003.

10 S. A. Hilderbrand and R. Weissleder, *Tetrahedron Lett.*, 2007, **48**, 4383–4385.

11 G. Pohlers, J. Scaiano and R. Sinta, *Chem. Mater.*, 1997, **9**, 3222–3230.

12 M. T. Ahmad, A. King, D. K. Ko, B. H. Cha and J. Lee, *J. Phys. D: Appl. Phys.*, 2002, **35**, 1473–1476.

13 A. Ojida, I. Takashima, T. Kohira, H. Nonaka and I. Hamachi, *J. Am. Chem. Soc.*, 2008, **130**, 12095–12101.

14 T. Hideu, JP 56005480, Jpn, Tokyo, KohoChem. Abstr., 1981, 95, p. 80922b.

15 B. Karami, S. J. Hoseini, K. Eskandari, A. Ghasemi and H. Nasrabad, *Catal. Sci. Technol.*, 2012, **2**, 331–338.

16 P. Bansal, N. Kaur, C. Prakash and G. R. Chaudhary, *Vacuum*, 2018, **157**, 9–16.

17 M. Seyyedhamzeh, P. Mirzaei and A. Bazgir, *Dyes Pigm.*, 2008, **76**, 836–839.

18 B. Karami, S. Nejati and K. Eskandaric, *Curr. Chem. Lett.*, 2015, **4**, 169–180.

19 N. Hazeri, A. Masoumnia, M. T. Mghsoodlou, S. Salahi, M. Kangani, S. Kianpour, S. Kiaee and J. Abonajmi, *Res. Chem. Intermed.*, 2015, **41**, 4123–4131.

20 S. Kantevari, R. Bantu and L. Nagarapu, *J. Mol. Catal. A: Chem.*, 2007, **269**, 53–57.

21 Z. H. Zhang and Y. H. Liu, *Catal. Commun.*, 2008, **9**, 1715–1719.

22 B. Das, P. Thirupathi, K. R. Reddy, B. Ravikanth and L. Nagarapu, *Catal. Commun.*, 2007, **8**, 535–538.

23 H. R. Shaterian, A. Hosseinian and M. Ghashang, *Phosphorus, Sulfur Silicon Relat. Elem.*, 2008, **183**, 3136–3144.

24 X. Fan, X. Hu, X. Zhang and J. Wang, *Can. J. Chem.*, 2005, **83**, 16–20.

25 D. H. Jung, Y. R. Lee, S. H. Kim and W. S. Lyoo, *Bull. Korean Chem. Soc.*, 2009, **30**, 1989–1995.

26 T. S. Jin, J. S. Zhang, A. Q. Wang and T. S. Li, *Synth. Commun.*, 2005, **35**, 2339–2345.

27 F. Nemati and S. Sabaqian, *J. Saudi Chem. Soc.*, 2017, **21**, S383–S393.

28 A. Amoozadeh, S. Golian and S. Rahmani, *RSC Adv.*, 2015, **5**, 45974–45982.

29 A. Amoozadeh, S. Rahmani, M. Bitaraf, F. B. Abadi and E. Tabrizian, *New J. Chem.*, 2016, **40**, 770–780.

30 J. Ma, X. Zhou, X. Zhang, C. Wang, Z. Wang, J. Li and Q. Li, *Aust. J. Chem.*, 2007, **60**, 146–148.

31 M. Dabiri, M. Baghbanzadeh and E. Arzroomchilar, *Catal. Commun.*, 2008, **9**, 939–942.

32 T. S. Jin, L. B. Liu, Y. Zhao and T. S. Li, *Synth. Commun.*, 2005, **35**, 2379–2385.

33 T. S. Jin, J. S. Zhang, A. Q. Wang and T. S. Li, *Ultrason. Sonochem.*, 2006, **13**, 220–224.

34 G. I. Shakibaei, P. Mirzaei and A. Bazgir, *Appl. Catal., A*, 2007, **325**, 188–192.

35 B. Das, P. Thirupathi, I. Mahender, V. S. Reddy and Y. K. Rao, *J. Mol. Catal. A: Chem.*, 2006, **247**, 233–239.

36 M. Dabiri, S. Azimi and A. Bazgir, *Chem. Pap.*, 2008, **62**, 522–526.

37 G. Song, B. Wang, H. Luo and L. Yang, *Catal. Commun.*, 2007, **8**, 673–676.

38 A. Rahmati, *Chin. Chem. Lett.*, 2010, **21**, 761–764.

39 D. Q. Shi, Q. Y. Zhuang, J. Chen, X. S. Wang, S. J. Tu and H. W. Hu, *Chin. J. Org. Chem.*, 2003, **23**, 694–696.

40 S. Kantevari, R. Bantu and L. Nagarapu, *ARKIVOC*, 2006, **xvi**, 136–148.

41 P. Paliwal, S. R. Jetti, A. Bhatewara, T. Kadre and S. Jain, *ISRN Org. Chem.*, 2013, 526173, DOI: 10.1155/2013/526173.

42 J. Albadi, M. Keshavarz, M. Abedini and M. Khoshakhlagh, *J. Chem. Sci.*, 2013, **125**, 295–298.

43 S. R. Mousavi, H. R. Nodeh, E. Z. Afshari and A. Foroumadi, *Catal. Lett.*, 2019, **149**, 1075–1086.

44 P. Liu, J. W. Hao, S. J. Liang, G. L. Liang, J. Y. Wang and Z. H. Zhang, *Monatsh. Chem.*, 2016, **147**, 801–808.

45 F. Darviche, S. Balalaie, F. Chadegani and P. Salehi, *Synth. Commun.*, 2007, **37**, 1059–1066.

46 A. John, P. J. P. Yadav and S. Palaniappan, *J. Mol. Catal. A: Chem.*, 2006, **248**, 121–125.

47 H. R. Shaterian, M. Sedghipour and E. Mollashahi, *Res. Chem. Intermed.*, 2014, **40**, 1345–1355.

48 J. M. Khurana, A. Lumb, A. Chaudhary and B. Nand, *J. Heterocycl. Chem.*, 2014, **51**, 1747–1751.

49 Y. Li, B. Du, X. Xu, D. Shi and S. Ji, *Chin. J. Chem.*, 2009, **27**, 1563–1568.

50 N. G. Khaligh and F. Shirini, *Ultrason. Sonochem.*, 2015, **22**, 397–403.

51 Z. N. Tisseh, S. C. Azimi, P. Mirzaei and A. Bazgir, *Dyes Pigm.*, 2008, **79**, 273–275.

52 S. Ko and C. F. Yao, *Tetrahedron Lett.*, 2006, **47**, 8827–8829.

53 D. Liu, S. Zhou, J. Gao, L. Li and D. Xu, *J. Mex. Chem. Soc.*, 2013, **57**, 345–348.

54 N. K. Ojha, G. V. Zyryanov, A. Majee, V. N. Charushin, O. N. Chupakhin and S. Santra, *Coord. Chem. Rev.*, 2017, **353**, 1–57.

55 M. B. Gawande, A. Goswami, F. X. Felpin, T. Asefa, X. Huang, R. Silva, X. Zou, R. Zboril and R. S. Varma, *Chem. Rev.*, 2016, **116**, 3722–3811.

56 B. Zeynizadeh, M. Zabihzadeh and Z. Shokri, *J. Iran. Chem. Soc.*, 2016, **13**, 1487–1492.

57 A. Alexakis, N. Krause and S. Woodward, *Copper-Catalyzed Asymmetric Synthesis*, Wiley-VCH, Weinheim, 2014.

58 F. Alonso, Y. Moglie, G. Radivoy and M. Yus, *Org. Biomol. Chem.*, 2011, **9**, 6385–6395.

59 J. M. Welter, *Copper: Better Properties for Innovative Products*, Wiley-VCH, Weinheim, 2007.

60 L. Yang, Y. Xie, H. Zhao, X. Wu and Y. Wang, *Solid-State Electron.*, 2005, **49**, 1029–1033.

61 L. Luo, Q. Li, Y. Xu, Y. Ding, X. Wang, D. Deng and Y. Xu, *Sens. Actuators, B*, 2010, **145**, 293–298.

62 P. Sivakumar, R. Ramesh, A. Ramanand, S. Ponnusamy and C. Muthamizhchelvan, *J. Alloys Compd.*, 2013, **563**, 6–11.

63 A. Ren, C. Liu, Y. Hong, W. Shi, S. Lin and P. Li, *Chem. Eng. J.*, 2014, **258**, 301–308.

64 A. S. A. Bakr, Y. M. Moustafa, E. A. Motawea, M. M. Yehia and M. M. H. Khalil, *J. Environ. Chem. Eng.*, 2015, **3**, 1486–1496.

65 B. Zeynizadeh, I. Mohammadzadeh, Z. Shokri and S. A. Hosseini, *J. Colloid Interface Sci.*, 2017, **500**, 285–293.

66 O. S. Ahmed and D. K. Dutta, *Langmuir*, 2003, **19**, 5540–5541.

67 B. J. Borah, D. Dutta, P. P. Saikia, N. C. Barua and D. K. Dutta, *Green Chem.*, 2011, **13**, 3453–3460.

68 P. P. Sarmah and D. K. Dutta, *Green Chem.*, 2012, **14**, 1086–1093.

69 A. Usuki, N. Hasegawa, H. Kadoura and T. Okamoto, *Nano Lett.*, 2001, **1**, 271–272.

70 B. S. Kumar, A. Dhakshinamoorthy and K. Pitchumani, *Catal. Sci. Technol.*, 2014, **4**, 2378–2396.

71 P. Malla, P. Ravindranathan, S. Komarneni and R. Roy, *Nature*, 1991, **351**, 555–557.

72 S. Karami, B. Zeynizadeh and Z. Shokri, *Cellulose*, 2018, **25**, 3295–3305.

73 B. Zeynizadeh and S. Rahmani, *RSC Adv.*, 2019, **9**, 8002–8015.

74 S. Rahmani and B. Zeynizadeh, *Res. Chem. Intermed.*, 2019, **45**, 1227–1248.

75 B. Zeynizadeh, S. Rahmani and E. Eghbali, *Polyhedron*, 2019, **168**, 57–66.

76 B. Zeynizadeh, S. Rahmani and S. Ilkhanizadeh, *Polyhedron*, 2019, **168**, 48–56.

77 D. Dutta, B. J. Borah, L. Saikia, M. G. Pathak, P. Sengupta and D. K. Dutta, *Appl. Clay Sci.*, 2011, **53**, 650–656.

78 B. Sahin and T. Kaya, *Appl. Surf. Sci.*, 2016, **362**, 532–537.

79 E. Şennik, S. Kerli, Ü. Alver and Z. Z. Öztürk, *Sens. Actuators, B*, 2015, **216**, 49–56.

80 S. K. Bhorodwaj and D. K. Dutta, *Appl. Catal., A*, 2010, **378**, 221–226.

81 S. Brunauer, L. S. Deming, W. E. Deming and E. Teller, *J. Am. Chem. Soc.*, 1940, **62**, 1723–1732.

82 J. Ji, P. Zeng, S. Ji, W. Yang, H. Liu and Y. Li, *Catal. Today*, 2010, **158**, 305–309.

83 P. K. Saikia, P. P. Sarmah, B. Borah, L. Saikia, K. Saikia and D. K. Dutta, *Green Chem.*, 2016, **18**, 2843–2850.

84 S. K. Bhorodwaj, M. G. Pathak and D. K. Dutta, *Catal. Lett.*, 2009, **133**, 185–191.

85 B. Tyagi, C. D. Chudasama and R. V. Jasra, *Appl. Clay Sci.*, 2006, **31**, 16–28.

86 J. Madejova and P. Komadel, *Clays Clay Miner.*, 2001, **49**, 410–432.

87 K. Wang, L. Wang, J. Wu, L. Chen and C. He, *Langmuir*, 2005, **21**, 3613–3618.

88 M. Mekewi, A. Darwish, M. Amin, G. Eshaq and H. Bourazan, *Egypt. J. Pet.*, 2016, **25**, 269–279.

89 R. Das, S. S. Nath and R. Bhattacharjee, *J. Fluoresc.*, 2011, **21**, 1165–1170.

90 B. Bagchi, S. Kar, S. K. Dey, S. Bhandary, D. Roy, T. K. Mukhopadhyay, S. Das and P. Nandy, *Colloids Surf., B*, 2013, **108**, 358–365.

91 K. R. Reddy, W. Park, B. C. Sin, J. Noh and Y. Lee, *J. Colloid Interface Sci.*, 2009, **335**, 34–39.